3D-Tracking of Sand Particles in a Wave Flume Using Interferometric Imaging

Marc Brunel, Lila Ouldarbi, Alexandre Fahy, Gaële Perret

optics

MDPI

Article

3D-Tracking of Sand Particles in a Wave Flume Using Interferometric Imaging

Marc Brunel [1,*], Lila Ouldarbi [1], Alexandre Fahy [1] and Gaële Perret [2]

[1] UMR CNRS 6614-CORIA, Normandie Université, BP 12, 76801 Saint-Etienne-du-Rouvray, France
[2] UMR CNRS 6294 LOMC, 53 Rue Prony, BP 540, 76058 Le Havre, France
* Correspondence: marc.brunel@coria.fr

Abstract: We report the 3D-tracking of irregular sand particles in a wave flume using a cylindrical interferometric particle imaging set-up. The longitudinal position of each particle is deduced from the ellipticity of its speckle-like interferometric image. The size of a particle is determined from the analysis of the 2D Fourier transform of its defocused image. It is further possible to identify some rotation of the particles. Simulations accurately confirm the experimental determination of the different parameters (3D position and size of each particle).

Keywords: interferometric particle imaging; speckle; sand; gravity waves

check for updates

Citation: Brunel, M.; Ouldarbi, L.; Fahy, A.; Perret, G. 3D-Tracking of Sand Particles in a Wave Flume Using Interferometric Imaging. *Optics* **2022**, *3*, 254–267. https://doi.org/10.3390/opt3030025

Academic Editor: Thomas Seeger

Received: 6 July 2022
Accepted: 18 August 2022
Published: 22 August 2022

Publisher's Note: MDPI stays neutral with regard to jurisdictional claims in published maps and institutional affiliations.

1. Introduction

The 3D-tracking of particles in a flow has important applications in atmospheric studies and health, combustion, sprays, and fluid dynamics [1–5]. The possibility to perform a 3D-tracking of particles using only one camera in a backward scattering configuration is very attractive when the optical access to the inner area of the flow is limited. Interferometric rough particle imaging can offer a solution in this case: it consists in the analysis of the speckle patterns produced by the particles under laser illumination [6–9]. It is an extension of Interferometric Laser Imaging for Droplet Sizing (ILIDS) [10–18] to the characterization of rough particles. However, in the case of rough particles, the technique is not limited to a small range of scattering angles, θ, as for droplets. ILIDS requires indeed that only the $p = 0$ (reflected ray) and $p = 1$ (transmitted ray without internal reflection). Debye orders dominate the scattering pattern produced by the droplet. It occurs at around $\theta = 70°$ for a water droplet with a perpendicular polarization of light (with respect to the incidence plane). With rough translucent particles, Interferometric Particle Imaging (IPI) can be used in a backward scattering configuration, as shown in different studies [9,19–21]. With sand particles, it has indeed been observed that the properties of the speckle pattern are independent on the scattering angle [8]. The technique could also be applied to the characterization of ice particles at scattering angles of 90°, or 135° as well [21,22]. IPI does not require the presence of a reference beam, as in digital holography [22]. Digital-in-line holography is a very convenient technique to perform a 3D-tracking of the particles, but the CCD sensor has to be in a forward scattering position, and not in a backward scattering position [23]. Other techniques such as stereo- and tomo-PIV have also been considerably developed in recent years to measure 3D velocity fields in flows, but they require the use of two or more cameras [24–26]. IPI delivers 2D images. To perform a 3D-tracking of particles and to obtain in particular their longitudinal position, a solution is to build a cylindrical imaging system [27–32]. It still works in a defocused configuration. Nevertheless, the defocused image of a particle is elliptical and its ellipticity is linked to the longitudinal position of the particle. With an appropriate design of the system, it is possible to define a region of interest where the 3D position of each particle is deduced from its defocused image. Analyzing the interferometric pattern in further detail, the size of the particle can be deduced as well.

Such a set-up can have different applications, but most of the experimental demonstrations have been performed on optical tables until now. The potentiality of the system still has to be validated on installations such as wind tunnels, or hydrodynamic channels. The present study will concern the tracking of sand particles in a wave flume. We will first demonstrate the possibility to simultaneously determine the 3D position of the particles and their size using a relatively simple instrumentation facing a Plexiglas window of the 35 m-long wave flume. Such a set-up has been proposed and tested previously on an optical table but not on a real hydrodynamic installation. The method will then be applied on a series of successive images to perform the tracking of the particles in the wave flume. The morphodynamics of the sea bottom is indeed strongly influenced by the size and shape of sedimentary particles. The understanding of particles' trajectory and deposit as a function of their size and shape is an important issue [33]. Moreover, in the sea, the performances of tidal turbines suffer the advection of stones of various sizes through the turbine. The possibility to measure the size, the trajectory, and the velocity of surrounding particles is important to evaluate the impacts and loads on the blades. We are interested here in the 3D-tracking of suspended sand particles in the presence of gravity waves. Experiments are performed in a wave flume and interferometric imaging is shown to enable a 3D-tracking of sand particles in suspension. Section 2 will first present the experimental set-up, while Section 3 will explain the cylindrical interferometric imaging method used to realize the 3D-tracking. Section 4 will show some results obtained concerning the 3D-tracking of the particles (Section 4.1), the measurement of the size of the sand particles using this cylindrical configuration (Section 4.2), and the rotation of a particle (Section 4.3).

2. Experimental Set-Up

ILIDS (corresponding to water droplets in air) is traditionally performed at the scattering angle of 70° (i.e., in a forward scattering region) [11]. The intensities of the reflected and refracted rays indeed have to be approximately equivalent to ensure an optimized contrast of the interferometric pattern. In addition, other scattering orders are then negligible. In the case of irregular rough particles, there is no such limitation, in particular for translucent particles such as sand. It is possible to work in a backscattering configuration. This property is directly linked to the measurement method: there is no theoretical model to predict the pattern scattered by irregular rough particles of any shape under coherent laser illumination. Nevertheless, in past studies, it has been assumed that a rough particle can be assimilated to an ensemble of coherent point emitters that cover the whole particle. In the Fresnel domain, the two-dimensional Fourier transform of the interferometric pattern is then demonstrated to be linked to the 2D autocorrelation of the envelope of the particle through Equation (1) [9]:

$$|FT_{2D}[I](\lambda B_{tot}u,\ \lambda B_{tot}v)| \ \propto\ |A_{2D}[G_0](dx,\ dy)| \tag{1}$$

where I is the intensity of the out-of-focus pattern of the particle and G_0 is the electric field scattered by the illuminated particle. λ is the wavelength of the laser, and λB_{tot} is the scaling factor between both functions, which is deduced from the set-up. Experimentally, this correspondence between the two-dimensional autocorrelation of the particle's shape with the two-dimensional Fourier transform ($2DFT$) of its interferometric image could be confirmed in many cases, in both backward and forward scattering regions [9,19–21]. This approach has offered the possibility to study and quantitatively interpret the interferometric scattered patterns.

To perform a 3D-tracking of the particles, the main difficulty is to determine the longitudinal position of the particles in the flow. One possibility is to measure the diameter of the defocused image of the particle using a classical imaging system. It is linked to the longitudinal position as the defocus parameter changes. Another possibility is to use a cylindrical defocused imaging system. The longitudinal position of the particle is then linked to the ellipticity of the defocused image of the particle [27–29], and specific

algorithms can be developed to determine the ellipticity of the defocused images [34]. This last solution based on a cylindrical imaging configuration is tested in the present work.

The interferometric imaging experiments reported in this study have been performed through the optical window of a 35 m-long, 90 cm-wide, and 1.2 m-high wave flume. A global top view of this channel is shown in Figure 1. Sand particles of varying size between 50 and 200 μm are deposited in the flume. Regular waves are generated by a piston-type wavemaker. The wave conditions have been chosen such that the particles remain in motion under wave action. The imaging set-up used to perform a 3D-tracking of the particles is shown in Figure 2. It consists of an enlarged laser beam sent into the channel through the window and an imaging system that collects light scattered by the sand particles in the backward region. The angle between the laser beam axis and the imaging axis is approximately 45° in this set-up (corresponding to a scattering angle of $\theta = 135°$ in a backward direction). The laser is a frequency-doubled Nd-YAG laser emitting nanosecond pulses at the wavelength of 532 nm. The detail of the imaging system is depicted in Figure 3. It is composed of a 200 mm focus length objective, a cylindrical lens (CL), a diaphragm (D), and a CCD sensor. The CCD sensor is made of 2048 × 2048 pixels (with a pixel size of 5.5 μm). The CCD sensor is synchronized with the laser to record bright interferometric images. As the pulse duration is very short, each image corresponds to a fixed position of the particle, without any blurring due to the particle's motion. The acquisition time of the CCD is 100 μs. The repetition rate of the laser illumination is 30 Hz. The time interval between two consecutive images is thus 33 ms. The laser beam is enlarged with an optical system to obtain a beam diameter of approximately 10 cm in the region of interest where the sand particles under study are located.

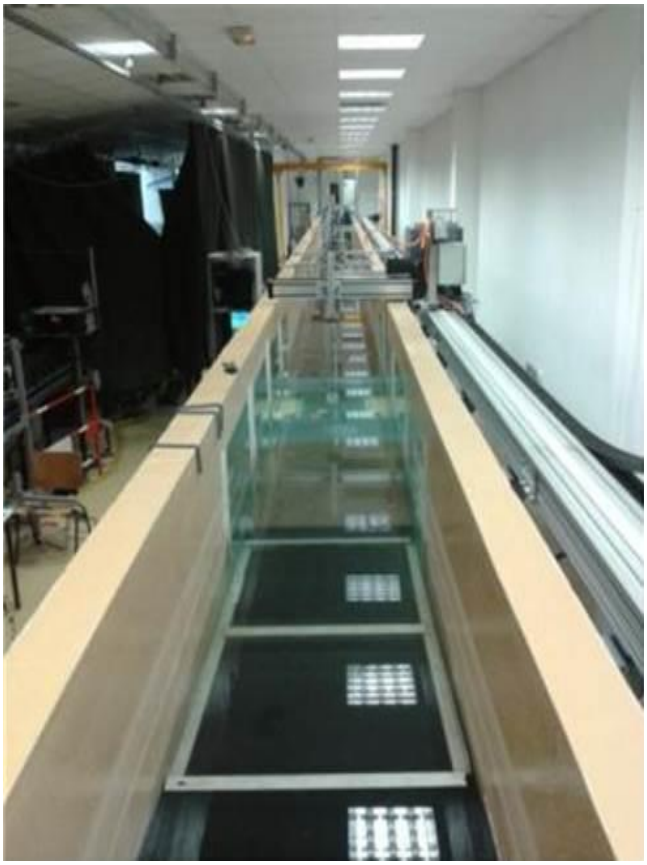

Figure 1. The wave flume.

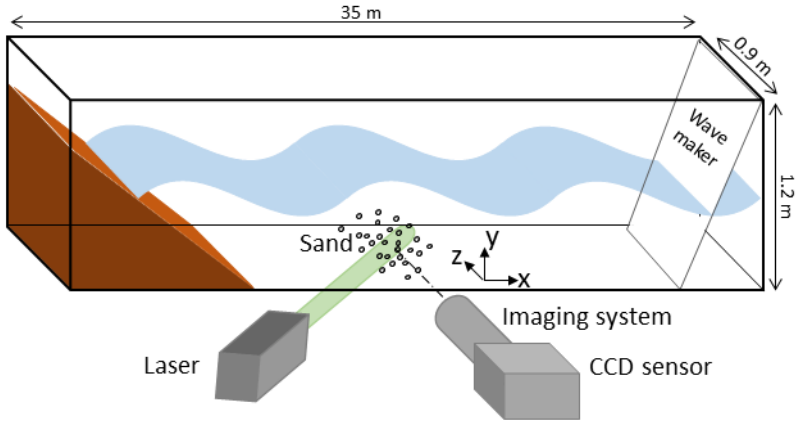

Figure 2. General experimental set-up.

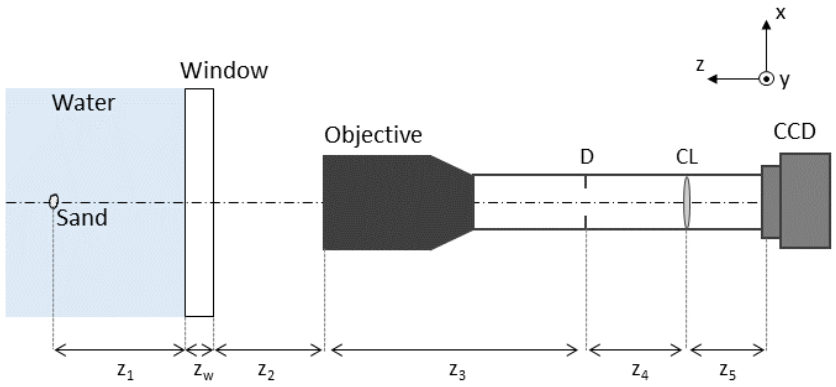

Figure 3. Experimental imaging set-up.

3. Method to Estimate the Longitudinal Particle's Coordinates

The transverse position of each particle will be deduced from the position of its out-of-focus image in the whole global image recorded with the CCD sensor. Let us now briefly recall the method used to determine the longitudinal position of a particle from its interferometric image. This is performed thanks to the cylindrical lens of the imaging system (CL in Figure 3). In the presence of the cylindrical lens, the interferometric image of each particle is no longer spherical, but elliptical. The ellipticity of this defocused image is linked to the longitudinal position z_1 of the particle. The determination of this z-coordinate is thus reduced to the determination of the ellipticity of the defocused interferometric image. For droplets in air or bubbles in water, the z-position of the particle can be further coupled to a rotation of the orientation of interference fringes to enhance the accuracy [27,28]. This is not possible with rough particles such as sand, whose interferometric images are complex speckle patterns.

Let us define the ellipticity of an interferometric out-of-focus image by the ratio Φ_y/Φ_x, where Φ_y is the size of the out-of-focus image along axis y while Φ_x is its size along axis x. This ratio is analytically linked to the parameters of the experimental set-up. Using a transfer matrix formalism through an optical system, in our case where the cylindrical lens is after the diaphragm we obtain [27–29]:

$$\frac{\Phi_y}{\Phi_x} = \left| \frac{B_T^y}{B_T^x} \right| \tag{2}$$

where B_T^x (respectively B_T^y) is the B coefficient of the total transfer matrix from the particle to the CCD sensor for transverse axis x (respectively for axis y). The parameters are $z_w = 20$ mm, $z_2 = 150$ mm, $f_{objective} = 200$ mm, $z_3 = 220$ mm, $z_4 = 72$ mm, and $z_5 = 60$ mm (see Figure 3 for the definition of these different parameters). The focus length

of the cylindrical lens (CL) is 100 mm for axis y, and infinite for axis x. The index of water is 1.33 and the index of the window is 1.5. With this set of parameters, Figure 4 shows the evolution of parameters B_T^x (in red) and B_T^y (in blue) versus parameter z_1 that gives the longitudinal position of the particle. Position z_1 corresponding to $B_T^y = 0$ corresponds to the position of the focused image for axis y. Position z_1 corresponding to $B_T^x = 0$ corresponds to the position of the focused image of the particle for axis x. Between these two values of z_1, a domain exists where the ellipticity of the defocused image varies from 0 to infinity versus z_1, as classicaly observed with astigmatic systems. Figure 5 shows the ratio Φ_y/Φ_x deduced from previous curves versus z_1. To illustrate these results, Figure 6 shows the simulation of four interferometric images of 200 µm rough particles, presenting 4 different longitudinal positions: $z_1 = 0.40$ m (a), $z_1 = 0.36$ m (b), $z_1 = 0.31$ m (c), and $z_1 = 0.27$ m (d). These simulations of particles' interferometric patterns are performed using the model developed in [7]. Each particle is assumed to be an ensemble of 30 coherent point emitters randomly located on a sphere of radius 100 µm. The electric field obtained in the plane of the CCD sensor is calculated using generalized Fresnel integrals. The coefficients of this integral are the coefficients of the optical transfer matrix of the set-up used. The aperture is described using a mathematical development of the hard-aperture D (defined in Figure 3) over a basis of gaussian functions [35,36], which enables the obtention of analytical relations [7].

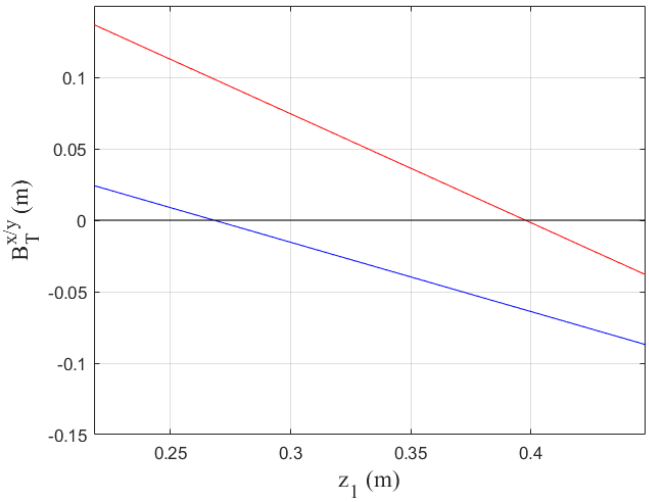

Figure 4. Evolution of the optical transfer matrix parameters B_T^x (in red) and B_T^y (in blue) versus the longitudinal position z_1 of the particle.

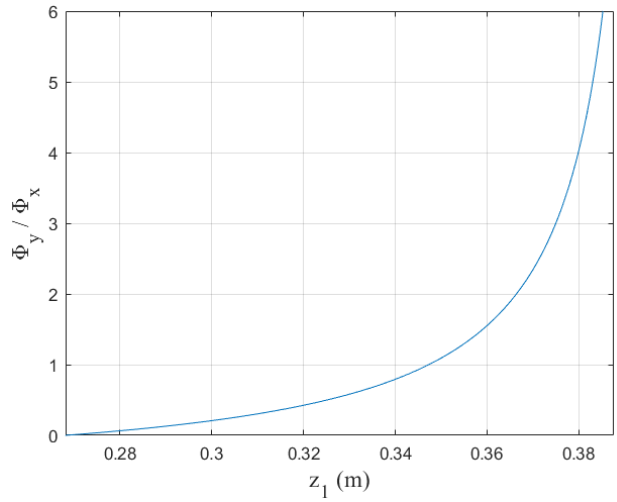

Figure 5. Evolution of the ellipticity ratio Φ_y/Φ_x of the interferometric image versus the longitudinal position z_1 of the particle under observation.

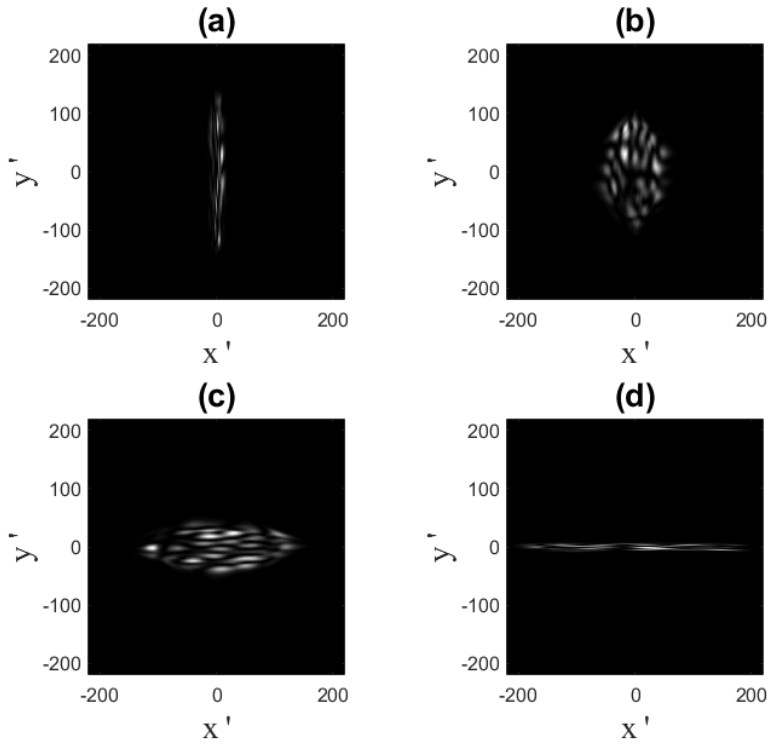

Figure 6. Interferometric images of 4 sand particles located at 4 different longitudinal positions: z_1 = 0.40 m (**a**), z_1 = 0.36 m (**b**), z_1 = 0.31 m (**c**), and z_1 = 0.27 m (**d**).

4. Experimental Results

4.1. 3D-Tracking of Particles

Let us now present the experimental results. Figure 7 shows an interferometric pattern recorded on the CCD sensor. Supplementary Video S1 shows a video composed of 20 images. The interferometric images observed evolve from vertical to horizontal segments, as predicted in Figure 6. In general, with ILIDS, we can detect and measure a few tens of particles per image (typically 20 or 30) depending on the value of the defocus parameter and of the field of view. Both parameters are actually adjusted to the concentration in particles when designing the system. Figure 7 contains approximately 20 particles. Some of them are on the longitudinal borders of the region of interest (interferometric images very similar to the plots of Figure 6a,b, respectively), and their quantitative analysis is not possible. The contrast of the images of some other particles can be very low. This is one of the main difficulties when transferring an experimental set-up from an optical table to an experimental system as a wave flume whose optical access is not high-quality optical windows. However, an analysis of the sequence can still be performed. We have decided here to follow 4 particles that are present on the 20 images of the sequence presented in Supplementary Video S1. To identify them easier in Figure 7 and in Supplementary Video S1, their interferometric images are "encircled" with an ellipse. As described in the theoretical section, the ellipticity of each defocused image provides the longitudinal position z_1 of the corresponding particle (the ellipticities have been determined for all images of Supplementary Video S1). Equation (2) shows that the ellipticity is linked to the optical transfer matrix coefficients of the imaging system. In the case of our set-up, Equation (2) used to plot Figure 5 is the equation of an hyperbole whose quantitative equation is Equation (3):

$$z_1(m) = 0.3976 - \frac{0.1294}{\Phi_y/\Phi_x/0.635 + 1} \tag{3}$$

where Φ_y/Φ_x is the ellipticity parameter of a defocused particle's image under study.

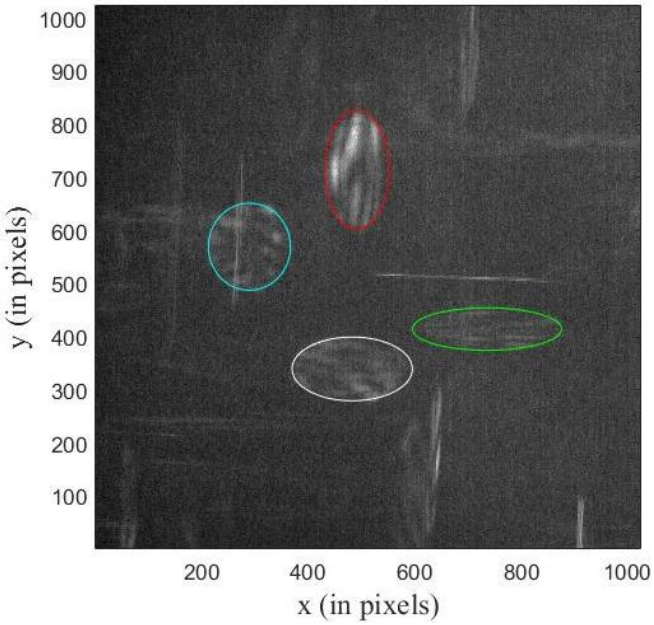

Figure 7. Interferometric images of sand particles in a wave flume. Four particles are selected to perform their 3D-tracking (Supplementary Video S1).

To perform a 3D-tracking of the different particles, the sole z_1 position of a particle is not sufficient. It is necessary to determine the x- and y-coordinates of each particle. As the imaging set-up is constituted of a cylindrical lens, the determination of these coordinates is not direct. For a defocused image, we first determine the coordinates $(x'_c,\ y'_c)$ of the center of the encircling ellipse. The transverse coordinates $(x_1,\ y_1)$ of the center of the particle (in the real measurement volume) are then provided by the relations:

$$x_1 = -\frac{B_1^x}{B_2^x}\, x'_c \tag{4}$$

$$y_1 = -\frac{B_1^y}{B_2^y}\, y'_c \tag{5}$$

where B_1^u is the B-coefficient of the optical transfer matrix from the sand particle to the aperture D (see Figure 3) for transverse axis u ($u = x$ or y), and B_2^u is the B-coefficient of the optical transfer matrix from the aperture D to the CCD sensor for transverse axis u ($u = x$ or y). Note that $B_1^x = B_1^y = B_1$ in our system. The cylindrical lens is indeed after the aperture D. Coefficients B_2^x and B_2^y are fixed by the set-up, but coefficient B_1 depends on the longitudinal position z_1 of the particle observed. For each particle of any image, we thus first determine the ellipticity of the out-of-focus image, deduce the z_1 position of the particle according to Equation (3), determine coefficient B_1 for this particle, and use Equations (4) and (5) to obtain the transverse coordinates $(x_1,\ y_1)$ of the particle. This is repeated for all particles selected and for all images. We can then perform a tracking of all particles selected. Figure 8 finally shows a tracking of the four particles selected in Figure 7 (and in Supplementary Video S1). The beginning of the trajectories during the tracking is represented by an encircled cross. As the time interval between the two consecutive images is 33 ms, it is actually possible to deduce the velocity of the particles from Figure 8.

4.2. Size Measurements of the Particles

IPI enables a deeper analysis than the sole 3D-tracking of the particles. It is indeed possible to determine the size of the particles. The procedure is as follows: For a given image (we will consider Figure 7), we select the defocused image of one particle. Let us first consider particle 1 (encircled in red in Figure 7). The selected pattern is reported in

Figure 9a. This truncated pattern is 2D Fourier-transformed. The reason for this operation is explained by Equation (1), which shows that the 2D Fourier transform of the interferometric image can be assimilated to the 2D autocorrelation of the contour of the rough particle. The procedure is, however, not as straightforward as usual. Equation (1) is indeed adapted to a spherical imaging set-up. In the case of a cylindrical imaging set-up, Equation (1) has to be modified, as:

$$\left|FT_{2D}[I]\left(\lambda B_{tot}^{x}u,\ \lambda B_{tot}^{y}v\right)\right| \ \propto\ |A_{2D}[G_0](dx,\ dy)| \tag{6}$$

where the scaling factors λB_{tot}^{x} and λB_{tot}^{y} are different, according to the cylindrical geometry of the set-up. B_{tot}^{x} and B_{tot}^{y} are the B-coefficients of the optical transfer matrix for the total system (i.e., from the particle to the CCD sensor), for both transverse axes x and y, respectively. It is actually possible to separately determine coefficients B_{tot}^{x} and B_{tot}^{y}. Their determination is carried out after determination of the longitudinal position z_1 of the particle. Table 1 summarizes all parameters obtained for the whole characterization of the particles tested. It will be detailed later. Figure 9b shows the 2D Fourier transform of the pattern in Figure 9a in the logarithmic scale, and after application of the two different scaling factors λB_{tot}^{x} and λB_{tot}^{y} along both transverse axes x and y. It is then binarized. The result is reported on Figure 9c. According to the modified Equation (6), this binarized shape can be assimilated to the 2D autocorrelation of the shape of this particle in Figure 7. Assuming an ellipsoidal shape of this particle, its dimensions are estimated to be 130 × 60 µm.

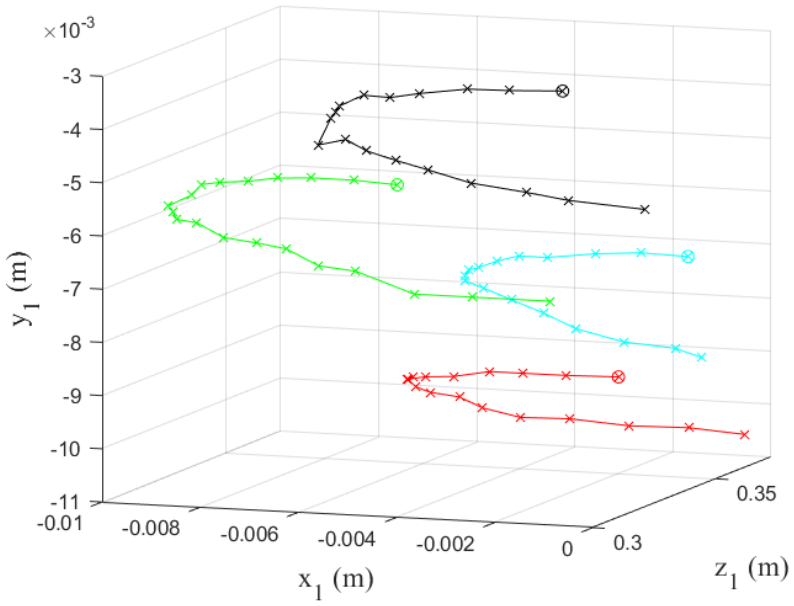

Figure 8. 3D-tracking of the 4 particles selected in Figure 7. (trajectories of particles 1, 2, 3, and 4 in red, green white and cyan respectively).

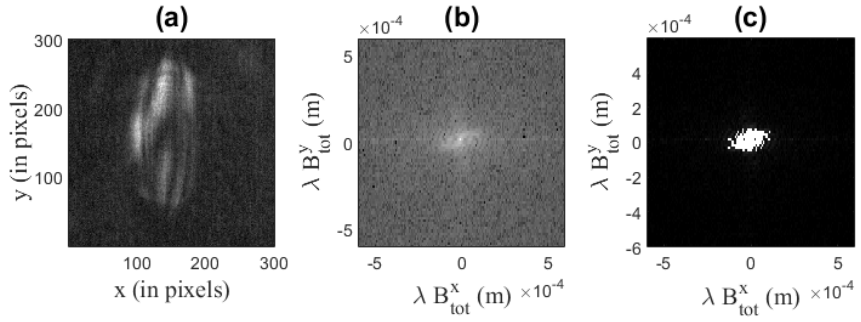

Figure 9. Section of the interferometric image of particle 1 (in red in Figure 7) that will be 2D Fourier-transformed (**a**), the log of its 2D Fourier transform (**b**), and its binarization (**c**).

Table 1. Parameters deduced during the analysis of the 4 "encircled" particles of Figure 7.

	Particle 1	**Particle 2**	**Particle 3**	**Particle 4**
color	red	green	white	cyan
Ellipticity $\frac{\Phi_y}{\Phi_x}$	1.87	0.29	0.53	1.06
z_1 (m)	0.365	0.308	0.327	0.349
x_1 (m)	−0.0047	−0.0073	−0.0047	−0.0028
y_1 (m)	−0.0103	−0.0062	−0.0050	−0.0083
B^x_{tot} (m)	0.0230	0.066	0.052	0.035
B^y_{tot} (m)	−0.047	−0.019	−0.029	−0.039
$(x \times y)$ size	130 × 60 µm	130 × 180 µm	140 × 170 µm	140 × 150 µm

This work is repeated for particle 2, encircled in green in Figure 7. The selected pattern, its scaled 2D Fourier transform in the logarithmic scale, and its binarization are presented in Figure 10a–c, respectively. In this case, the dimensions of the particle are estimated to be 130 × 180 µm.

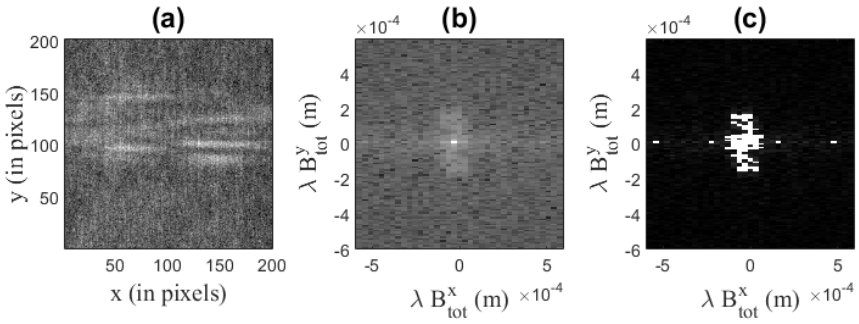

Figure 10. Section of the interferometric image of particle 2 (in green in Figure 7) that will be 2D Fourier-transformed (**a**), the log of its 2D Fourier transform (**b**), and its binarization (**c**).

For particle 3 (encircled in white in Figure 7), the truncated pattern, its scaled 2D Fourier transform in the logarithmic scale, and its binarization are presented in Figure 11a–c, respectively. The dimensions of the particle can be estimated to be 140 × 170 µm.

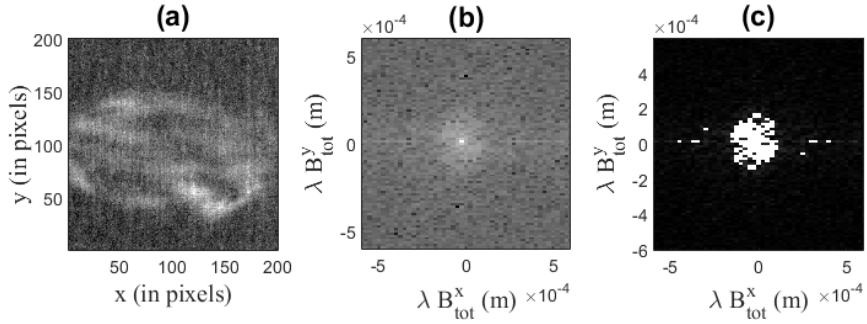

Figure 11. Section of the interferometric image of particle 3 (in white in Figure 7) that will be 2D Fourier-transformed (**a**), the log of its 2D Fourier transform (**b**), and its binarization (**c**).

For particle 4 (encircled in cyan in Figure 7), the results are presented in a similar form in Figure 12. The dimensions of the particle can be estimated to be 140 × 150 µm. This last case shows a supplementary difficulty. The defocused image of another particle is indeed superposed to the pattern of Figure 12a (the sharp vertical lines). It induces more noise on the horizontal axis of Figure 12b,c after 2D Fourier transform. Nevertheless,

eliminating these sharp horizontal extensions on the 2D Fourier transforms of Figure 12b,c, an estimation of the dimensions of the particle can be performed.

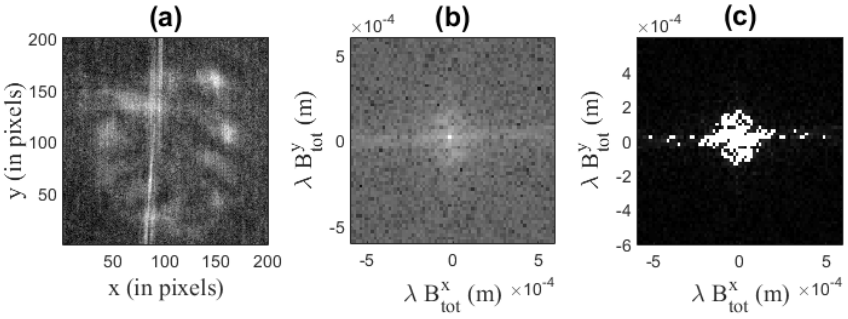

Figure 12. Section of the interferometric image of particle 4 (in cyan in Figure 7) that will be 2D Fourier-transformed (**a**), the log of its 2D Fourier transform (**b**), and its binarization (**c**).

In order to summarize the whole study for the four selected particles of Figure 7, Table 1 shows, for each particle: the ellipticity of its defocused image, the longitudinal position of the particle (z_1), the transverse position of the particle (x_1 and y_1), coefficients B^x_{tot} and B^y_{tot}, and the size of the particle, assuming an ellipsoidal shape.

Using these parameters, it is possible to predict the interferometric images of these four particles. The four particles are assumed to be composed of coherent point emitters randomly located on the surface of the particle. They are plotted in Figure 13a–d and match the dimensions predicted for particles 1, 2, 3, and 4, respectively. As in Section 4 to obtain Figure 6, the simulation of the interferometric pattern is performed using the model developed in [7]. The image obtained is presented in Figure 14. We can see that this simulation created using the parameters obtained during the analysis of the experimental image affords a pattern very similar to the experimental one.

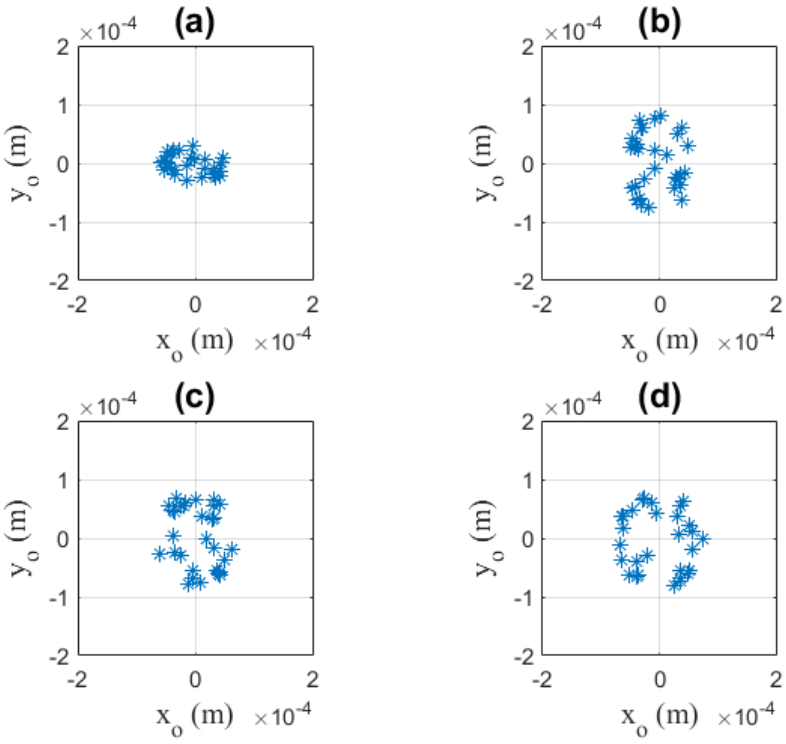

Figure 13. Particles 1 (**a**), 2 (**b**), 3 (**c**), and 4 (**d**) represented by an ensemble of coherent point emitters randomly located on the binarized shapes obtained in Figures 9c, 10c, 11c and 12c, respectively.

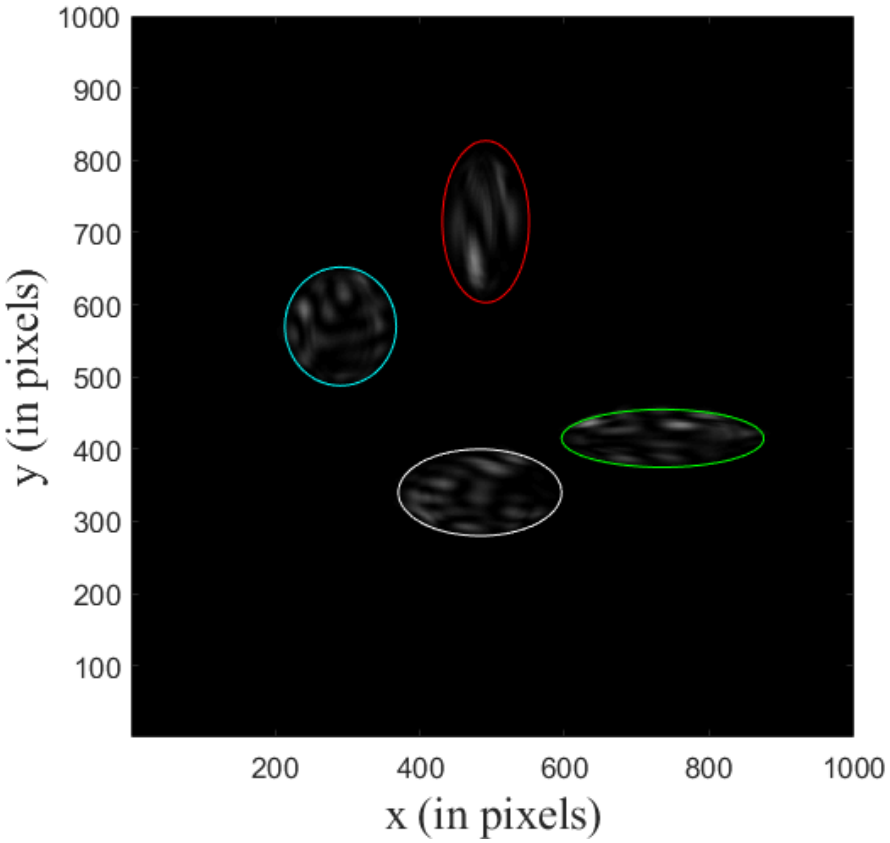

Figure 14. Interferometric pattern simulated with the interferometric images of particles 1, 2, 3, and 4 of Figure 13, whose positions, sizes, and shapes have been deduced from the whole analysis.

4.3. Rotation of Particles

During the experiment, the sand particles might not only move and form trajectories as in Figure 8, they can also rotate since they are not perfect spheres. One can wonder whether it is possible to visualize this effect.

The first problem in answering this question is that we observe speckle patterns whose 2D Fourier transform can be assimilated to the 2D autocorrelation of the shape of the particle (according to Equations (1) and (6)). Unfortunately, the 2D autocorrelation of a 2D shape does not give the original 2D shape directly. Phase retrieval algorithms can be a solution to reconstruct the exact 2D shape [37–39]. However, it still needs to be confirmed with the experimental patterns of real particles in a flow. Demonstrations have only been carried out on simulated patterns or on the experimental patterns produced by particles programmed on a Digital Micromirror Device [38,39].

The second problem is that the rotation of the particle is not necessarily around the z-axis (the interferometric images presented in the paper correspond to the (x,y)-plane). The rotation axis could have any other direction depending on the real 3D shape of the particle. More angles of view would be necessary to perform a real tomography of the particles [39].

Nevertheless, assuming that the sand particles of our experiment can be assimilated to ellipsoidal particles, Figure 15 will show that it is possible to detect a rotation of a particle during its displacement in the wave flume. Figure 15 shows some images recorded during another sequence of acquisition. In this sequence, we isolate the displacement of only one sand particle. Figure 15a,c,e present the interferometric images of the same particle at three different times (0.47, 0.57, and 0.77 s, respectively). The global trajectory followed by the particle is indicated with the white curve that has been added. Figure 15b,d,f present the binarized 2D Fourier transforms of the interferometric images of Figure 15a,c,e, respectively. The scaling factors have been applied along both the x- and y-axis according to Equation (6).

We thus observe the binarized 2D autocorrelations of the 2D shape of the particle at the three times of 0.47, 0.57, and 0.77 s, respectively. Assuming that the sand particles of our experiment are ellipsoidal particles, we can clearly identify a rotation of (0.07π) of the particle in the flow at this stage of the trajectory (between Figures 15a and 15c), and of (-0.07π) between Figures 15c and 15e. The red lines present the main axis of the "ellipsoidal" contours plotted in Figure 15b,d,f.

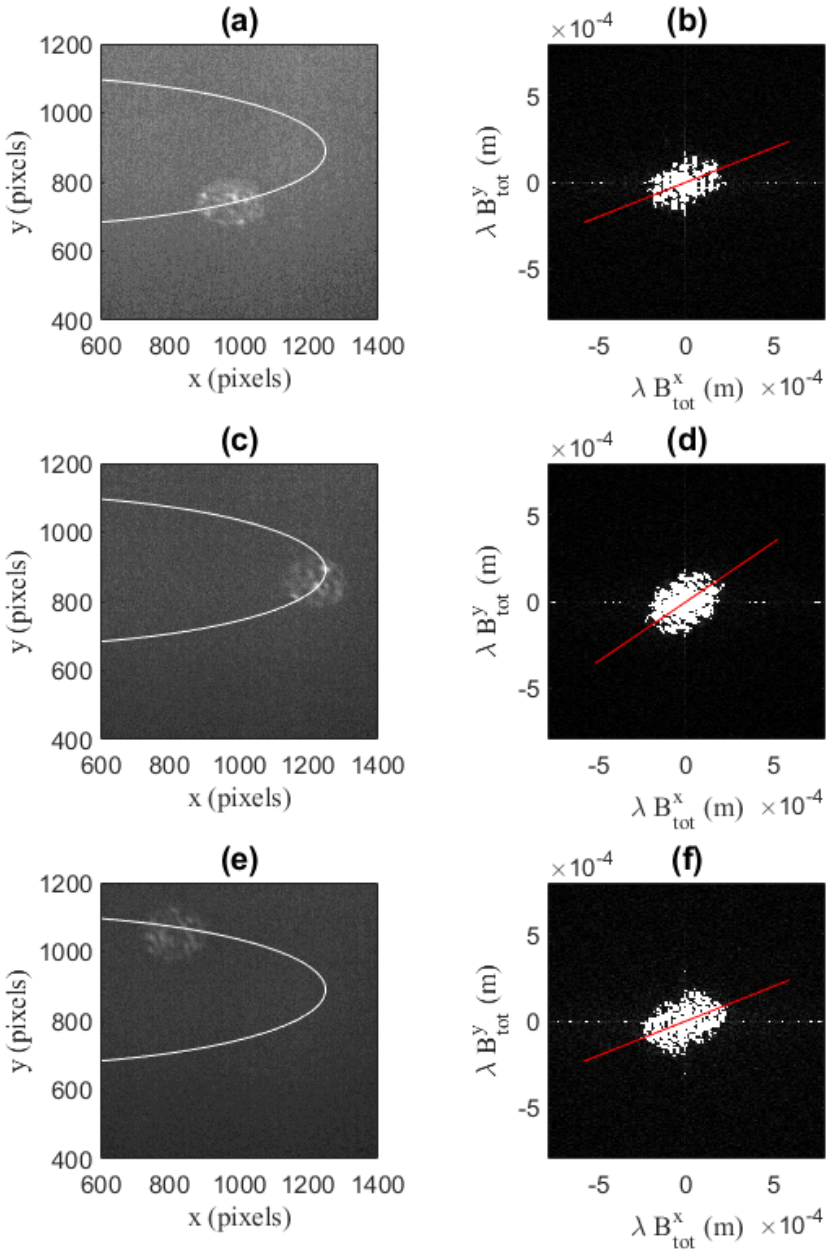

Figure 15. Interferometric images of the same particle at three different times: 0.47 s (**a**), 0.57 s (**c**), and 0.77 s (**e**), and their binarized 2D Fourier transforms in (**b**,**d**,**f**), respectively. The white curves in (**a**,**c**,**e**) present the global trajectory of the particle.

5. Conclusions

This study showed the 3D-tracking of irregular rough sand particles in a wave flume using a backward scattering configuration and only one camera. The 3D-tracking was obtained using a cylindrical interferometric particle imaging set-up. A sole image enabled the 3D location and the measurement of the size of the particles. The longitudinal position of each particle was deduced from the ellipticity of its speckle-like interferometric image.

The size of a particle was determined from the analysis of the 2D Fourier transform of its defocused image. It was further possible to identify some rotation of the particles. The 3D-tracking was then performed from image to image at the repetition rate of the laser system that illuminates the region of interest. The experimental results obtained were described and interpreted precisely using a scattering model that assimilates the sand particles to a collection of coherent point emitters that cover the particle. Simulations accurately confirmed the experimental determination of the different parameters (3D position and size of each particle). The design of prototypes that could perform measurements in the vicinity of tidal turbines or sedimentary bottom is thus possible using this technique.

As for ice crystals in icing wind tunnels [40], this work showed the possibility to characterize rough particles in complex flows and large instruments using IPI, i.e., sand particles in wave flumes in this study. Recent studies have shown that the analysis of the interferometric images of rough particles could be refined using phase retrieval algorithms [37–39]. Future works should thus lead to a better reconstruction of the particle's shapes using this technique, that requires only the record of light scattered by the particles after a laser pulse illumination, without the addition of any reference beam.

Supplementary Materials: The following supporting information can be downloaded at: https://www.mdpi.com/article/10.3390/opt3030025/s1, Video S1: Interferometric images of sand particles in a wave flume.

Author Contributions: Experiments, L.O. and G.P.; investigation and data curation, L.O., A.F., G.P. and M.B.; writing—review and editing, M.B.; funding acquisition, M.B. and G.P. All authors have read and agreed to the published version of the manuscript.

Funding: Authors acknowledge Agence Nationale de la Recherche for EMC3 LABEX project "3D".

Institutional Review Board Statement: Not applicable.

Informed Consent Statement: Not applicable.

Data Availability Statement: Data underlying the results presented in this paper are not publicly available at this time but may be obtained from the authors upon reasonable request.

Conflicts of Interest: The authors declare no conflict of interest.

References

1. Chang, T.; Tatterson, G. Application of image processing to the analysis of three-dimensional flow fields. *Opt. Eng.* **1983**, *23*, 283–287. [CrossRef]
2. Agüi, J.C.; Jimenez, J. On the performance of particle tracking. *J. Fluid Mech.* **1987**, *185*, 447–468. [CrossRef]
3. Maas, H.G.; Gruen, A.; Papantoniou, D. Particle tracking velocimetry in three-dimensional flows. *Exp. Fluids* **1993**, *15*, 133–146. [CrossRef]
4. Ohmi, K.; Li, H.-Y. Particle-tracking velocimetry with new algorithms. *Meas. Sci. Technol.* **2000**, *11*, 603. [CrossRef]
5. Hoyer, K.; Holzner, M.; Lüthi, B.; Guala, M.; Liberzon, A.; Kinzelbach, W. 3D scanning particle tracking velocimetry. *Exp. Fluids* **2005**, *39*, 923S–934S. [CrossRef]
6. Ouldarbi, L.; Pérret, G.; Lemaitre, P.; Porcheron, E.; Coëtmellec, S.; Gréhan, G.; Lebrun, D.; Brunel, M. Simultaneous 3D location and size measurement of bubbles and sand particles in a flow using interferometric particle imaging. *Appl. Opt.* **2015**, *54*, 7773–7780. [CrossRef]
7. Brunel, M.; Shen, H.; Coëtmellec, S.; Gréhan, G.; Delobel, T. Determination of the size of irregular particles using interferometric out-of-focus imaging. *Int. J. Opt.* **2014**, *2014*, 143904. [CrossRef]
8. García Carrascal, P.; González Ruiz, S.; van Beeck, J.P.A.J. Irregular particle sizing using speckle pattern for continuous wave laser applications. *Exp. Fluids* **2014**, *55*, 1851. [CrossRef]
9. Brunel, M.; González Ruiz, S.; Jacquot, J.; van Beeck, J. On the morphology of irregular rough particles from the analysis of speckle like interferometric out-of-focus images. *Opt. Commun.* **2015**, *338*, 193–198. [CrossRef]
10. König, G.; Anders, K.; Frohn, A. A new light-scattering technique to measure the diameter of periodically generated moving droplets of the article. *J. Aerosol Sci.* **1986**, *17*, 157–167. [CrossRef]
11. Glover, A.R.; Skippon, S.M.; Boyle, R.D. Interferometric laser imaging for droplet sizing: A method for droplet-size measurement in sparse spray systems. *Appl. Opt.* **1995**, *34*, 8409–8421. [CrossRef] [PubMed]
12. Mounaïm-Rousselle, C.; Pajot, O. Droplet sizing by Mie scattering interferometry in a spark ignition engine. *Part. Part. Syst. Charact.* **1999**, *16*, 160–168. [CrossRef]

13. Kawaguchi, T.; Akasaka, Y.; Maeda, M. Size measurements of droplets and bubbles by advanced interferometric laser imaging technique. *Meas. Sci. Technol.* **2002**, *13*, 308. [CrossRef]
14. Damaschke, N.; Nobach, H.; Tropea, C. Optical limits of particle concentration for multi-dimensional particle sizing techniques in fluid mechanics. *Exp. Fluids* **2002**, *32*, 143–152.
15. Dehaeck, S.; van Beeck, J.P.A.P. Designing a maximum precision interferometric particle imaging set-up. *Exp. Fluids* **2007**, *42*, 767–781. [CrossRef]
16. Volkov, R.S.; Kuznetsov, G.V.; Strizhak, P.A. Influence of droplet concentration on evaporation in a high-temperature gas. *Int. J. Heat Mass Transf.* **2016**, *96*, 20. [CrossRef]
17. Zhang, H.; Zhou, Y.; Liu, J.; Jia, D.; Liu, T. A new method for determining the sampling volume and the number of particles within it for particle concentration identification in defocused Interferometric Particle Imaging. *IEEE Photonics J.* **2017**, *9*, 6801015. [CrossRef]
18. Garcia-Magarino, A.; Sor, S.; Bardera, R.; Munoz-Campillejo, J. Interferometric laser imaging for droplet sizing method for long range measurements. *Measurement* **2021**, *168*, 108418. [CrossRef]
19. Ruiz, S.G.; van Beeck, J. Sizing of sand and ash particles using their speckle pattern: Influence of particle opacity. *Exp. Fluids* **2017**, *58*, 100. [CrossRef]
20. Wu, Y.; Gong, Y.; Shi, L.; Lin, Z.; Wu, X.; Gong, C.; Zhou, Z.; Zhang, Y. Backward interferometric speckle imaging for evaluating size and morphology of irregular coal particles. *Opt. Commun.* **2021**, *491*, 126957. [CrossRef]
21. Talbi, M.; Gréhan, G.; Brunel, M. Interferometric particle imaging of ice particles using a multi-view optical system. *Appl. Opt.* **2018**, *57*, 6188–6197. [CrossRef] [PubMed]
22. Jacquot-Kielar, J.; Wu, Y.; Coëtmellec, S.; Lebrun, D.; Gréhan, G.; Brunel, M. Size determination of mixed liquid and frozen water droplets using interferometric out-of-focus imaging. *J. Quant. Spectrosc. Radiat. Transf.* **2016**, *178*, 108–116. [CrossRef]
23. Murata, N.; Yasuda, N. Potential of digital holography in particle measurement. *Opt. Las. Technol.* **2000**, *32*, 567–574. [CrossRef]
24. Lebon, B.; Perret, G.; Coëtmellec, S.; Godard, G.; Gréhan, G.; Lebrun, D.; Brossard, J. A digital holography set-up for 3D vortex flow dynamics. *Exp. Fluids* **2016**, *57*, 103. [CrossRef]
25. Sarano, F. Tomographic PIV: Principles and practice. *Meas. Sci. Technol.* **2012**, *24*, 012001. [CrossRef]
26. Schröder, A.; Geisler, R.; Staack, K.; Elsinga, G.E.; Scarano, F.; Wieneke, B.; Henning, A.; Poelma, C.; Westerweel, J. Eulerian and lagrangian views of a turbulent boundary layer flow using time-resolved tomographic PIV. *Exp. Fluids* **2011**, *50*, 1071–1091. [CrossRef]
27. Shen, H.; Coëtmellec, S.; Brunel, M. Cylindrical interferometric out-of-focus imaging for the analysis of droplets in a volume. *Opt. Lett.* **2012**, *37*, 3945–3947. [CrossRef]
28. Brunel, M.; Shen, H. Design of ILIDS configurations for droplet's characterization. *Particuology* **2013**, *11*, 148–157. [CrossRef]
29. Shen, H.; Coëtmellec, S.; Brunel, M. Simultaneous 3D location and size measurement of spherical bubbles using cylindrical interferometric out-of-focus imaging. *J. Quant. Spectrosc. Radiat. Transf.* **2013**, *131*, 153–159. [CrossRef]
30. Wu, Y.; Zhuo, Z.; Lin, Z.; Wen, B.; Wu, X.; Cen, K. Astigmatic dual-beam interferometric particle imaging for metal droplet 3D position and size measurement. *Opt. Lett.* **2021**, *46*, 1942–1945. [CrossRef]
31. Wen, B.; Wu, Y.; Zhuo, Z.; Wu, X. Characterization and verification of astigmatic interferometric particle imaging for volumetric droplet 3D position and size measurement. *Adv. Powd. Technol.* **2021**, *32*, 3476–3483. [CrossRef]
32. Zhuo, Z.; Wu, Y.; Wen, B.; Lin, Z.; Wu, X. Modeling and experiment on 3D position and size measurement of opaque droplet cloud with astigmatic dual-beam interferometric particle imaging (ADIPI). *Powd. Technol.* **2022**, *395*, 111–121. [CrossRef]
33. Durafour, M.; Jarno, A.; Le Bot, S.; Lafite, R.; Marin, F. Bedload transport for heterogeneous sediments. *Environ. Fluid Mech.* **2015**, *15*, 731–751. [CrossRef]
34. Lemaitre, P.; Ouldarbi, L.; Shen, H.; Porcheron, E.; van Beeck, J.; Gréhan, G.; Brunel, M. A new algorithm to determine the 3D location of particles in a flow using cylindrical interferometric out-of-focus imaging. *J. Flow Vis. Image Process.* **2015**, *22*, 131–150. [CrossRef]
35. Wen, J.J.; Breazeale, M. Gaussian beam functions as a base function set for acoustical field calculations. In Proceedings of the IEEE Ultrasonics Symposium, Denver, CO, USA, 14–16 October 1987; pp. 1137–1140.
36. Wen, J.J.; Breazeale, M. A diffraction beam expressed as the superposition of Gaussian beams. *J. Acoust. Soc. Am.* **1988**, *83*, 1752–1756. [CrossRef]
37. Fienup, R.; Crimmins, T.R.; Holsztynski, W. Reconstruction of the support of an object from the support of its autocorrelation. *J. Opt. Soc. Am.* **1982**, *7*, 3–13. [CrossRef]
38. Shen, H.; Wu, L.; Li, Y.; Wang, W. Two-dimensional shape retrieval from the interferometric out-of-focus image of a nonspherical particle—Part I: Theory. *Appl. Opt.* **2018**, *57*, 4968–4976. [CrossRef]
39. Delestre, B.; Abad, A.; Talbi, M.; Brunel, M. Tomography of irregular rough particles using the Error-Reduction algorithm with multiviews interferometric particle imaging. *J. Opt. Soc. Am. A* **2021**, *38*, 1237–1247. [CrossRef]
40. Talbi, M.; Duperrier, R.; Delestre, B.; Godard, G.; Brunel, M. Interferometric ice particle imaging in a wind tunnel. *Optics* **2021**, *2*, 216–227. [CrossRef]